Origami Crawlers
Exploring A Single Origami Vertex for Complex Path Navigation

Farhadi, Davood; Pernigoni, Laura; Melancon, David; Bertoldi, Katia

DOI
10.1002/adma.202502293

Publication date
2025

Document Version
Final published version

Published in
Advanced Materials

ADVANCED MATERIALS
www.advmat.de

Origami Crawlers: Exploring A Single Origami Vertex for Complex Path Navigation

Davood Farhadi, Laura Pernigoni, David Melancon, and Katia Bertoldi**

The ancient art of origami, traditionally used to transform simple sheets into intricate objects, also holds potential for diverse engineering applications, such as shape morphing and robotics. In this study, it is demonstrated that one of the most basic origami structures–a rigid, foldable degree-four vertex–can be engineered to create a crawler capable of navigating complex paths using only a single input. Through a combination of experimental studies and modeling, it is shown that modifying the geometry of a degree-four vertex enables sheets to move either in a straight line or turn. Furthermore, it is illustrated that leveraging the nonlinearities in folding allows the design of crawlers that can switch between moving straight and turning. Remarkably, these crawling modes can be controlled by adjusting the range of the folding angle's actuation. This study opens avenues for simple machines that can follow intricate trajectories with minimal actuation.

1. Introduction

While traditionally regarded as an art form, origami has recently made a profound impact on engineering applications, playing a pivotal role in the design of deployable and reconfigurable structures,[1–6], metamaterials with programmable responses[7–9] and mechanical logic elements.[10,11] Further, origami principles have provided an opportunity to simplify and accelerate the fabrication of robots, since they enable their manufacturing from a flat composite through folding.[12–17] Beyond simplifying the manufacturing process, origami has also enabled the design of grippers to encapsulate delicate specimens[18] and efficient crawlers.[19–23]

In applications, crawlers are typically required to follow arbitrary trajectories. This is commonly accomplished by employing multiple actuators, each assigned to a specific gait, and coordinated through control circuits.[14,24–26] The pursuit of simpler strategies for achieving locomotion along arbitrary trajectories remains a significant challenge in robotics.[27] In the case of soft machines, this challenge has been addressed by implementing actuation through a magnetic field[28,29] and by integrating pneumatic control circuits.[30,31] Conversely, for rigid-body linkages, diverse gaits from a single actuation have been successfully achieved by incorporating passive actuators to modify the effective length of the linkage.[32–34]

In this work, we leverage the highly nonlinear kinematics of origami to create a crawler capable of following complex trajectories with a single input. We focus on one of the simplest origami building blocks, the degree-four origami vertex,[35–37] and demonstrate through a combination of experiments and modeling how the position of the central vertex and the orientation of the creases significantly impact its crawling ability and resulting trajectory. Guided by our model, we identify designs that can move straight when the folding angle is actuated within a certain range and turn when actuated in another range. This enables the creation of simple machines that can follow complex trajectories by simply controlling the folding angle at the actuated crease.

2. Results

We consider a rectangular sheet with width b and height h and embed four creases to create a generic degree-four vertex (**Figure 1A**). The flat state configuration of the sheet is defined by four sector angles, θ_i ($i = 1, ..., 4$), the orientation of the creases with respect to the rectangular sheet, defined by the angle θ_v, and the position of the central vertex, specified by the coordinates (x_v, y_v). Our focus is on developable (for which $\sum\theta_i = 2\pi$) and rigidly foldable (for which. $\theta_j < \sum\theta_{i\neq j}$) configurations.[35] While these configurations may not always fulfill the flat foldability criterion (i.e., $\theta_1 + \theta_3 \neq \pi$), their kinematic is characterized by a single degree of freedom (Movie S1, Supporting Information). To actuate the origami sheet, we attach an inflatable pouch to the valley

D. Farhadi, L. Pernigoni, K. Bertoldi
J.A. Paulson School of Engineering and Applied Sciences
Harvard University
Cambridge, MA 02138, USA
E-mail: d.farhadimachekposhti@tudelft.nl; bertoldi@seas.harvard.edu
D. Farhadi
Department of Precision and Microsystems Engineering
Delft University of Technology
Mekelweg 2, 2628 CD Delft, The Netherlands
L. Pernigoni
Department of Aerospace Engineering
Politecnico di Milano
Milan 20133, Italy
D. Melancon
Laboratory for Multi-Scale Mechanics (LM2)
Department of Mechanical Engineering
Polytechnique Montreal
2500 chemin de Polytechnique
Montreal (Quebec) H3T1J6, Canada
The ORCID identification number(s) for the author(s) of this article can be found under https://doi.org/10.1002/adma.202502293

DOI: 10.1002/adma.202502293

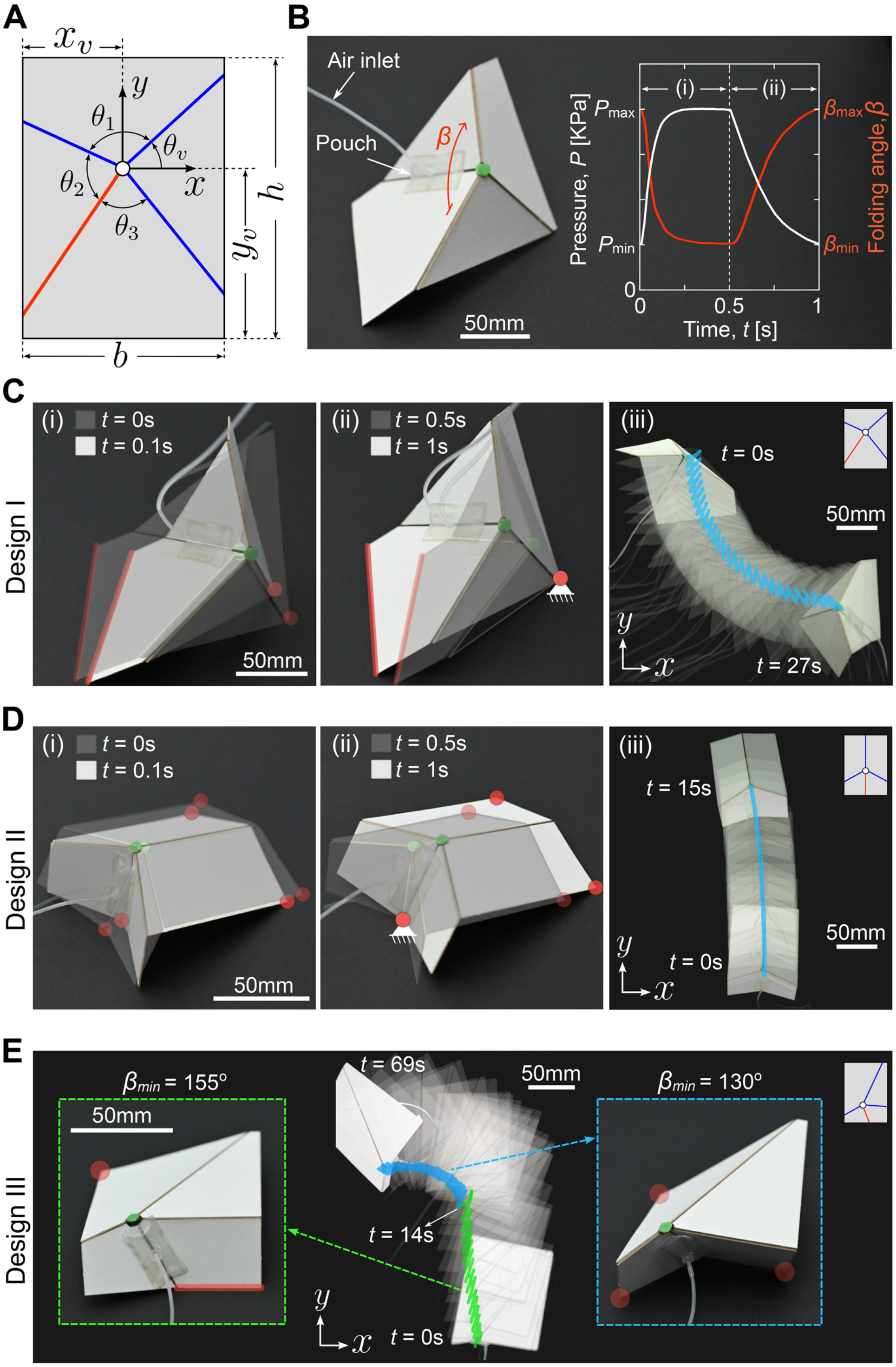

Figure 1. Multimodal crawling locomotion of a degree-four origami vertex. A) Schematic of a degree-four origami vertex with mountain folds (blue lines), and a valley fold (red line). B) Physical prototype actuated by pressurizing an inflatable pouch attached to the valley fold. The pressure profile used for actuation is shown on the right, together with the corresponding evolution of the folding angle β. C–E) Experimental results for C) Design I, D) Design II, and E) Design III. Snapshots of origami sheets at different times during loading cycles and frames from videos recorded during tests in which the samples were subjected to multiple inflation/deflation cycles.

crease (Figure 1B) and increase its pressure from P_{min} to P_{max} in 0.5 s. This inflation step is immediately followed by a deflation phase, in which the pressure is reduced back to P_{min} over 0.5 s. This applied pressure profile induces an asymmetric rate of change in the folding angle of the valley crease, β. As shown in Figure 1B, β rapidly decreases from β_{max} to β_{min} within 0.1 seconds during inflation and returns more gradually to β_{max} during deflation.

In Figure 1C,D, we show results for two different origami sheets, both with $b = 90$ mm, $h = 130$ mm, but different angles θ_i and θ_v as well as vertex coordinates. Specifically, Design I features an asymmetric pattern with angles (θ_1, θ_2, θ_3, θ_v)=(109°, 79°, 80°, 45°) and vertex coordinates $(x_v, y_v) = (45, 80)$ mm (Figure 1C). In contrast, Design II, characterized by angles (θ_1, θ_2, θ_3, θ_v)=(110°, 70°, 70°, 90°) and vertex coordinates $(x_v, y_v) = (45, 50)$ mm, exhibits an axis of symmetry aligned with the long edge of the sheet (Figure 1D).

In Figure 1C(i)-(ii), D(i)-(ii) we show snapshots of the origami sheets at $t = 0$, 0.1, 0.5, and 1 s, while in Figure 1C(iii),D(iii), we report frames recorded during tests in which we cyclically actuated the origami sheets. Note that a green marker is placed on the central vertex to track the motion of the samples. Four key observations can be made. First, the orientation of the creases significantly influences the folding of the sheet, thereby determining the location of its center of mass. This, in turn, dictates which edges and vertices are in contact with the substrate, as highlighted by the red lines and markers in Figure 1C(i) and the red markers in Figure 1D(i). Second, since the folding angle β rapidly decreases during inflation (Figure 1B), all contact points slip due to the dynamic nature of the process (Figure 1C(i),D(i)). Third, since the deflation process occurs at a comparatively slower rate (Figure 1B), contact points with higher static friction forces tend to stick and act as anchor points (Figure 1C(ii),D(ii)). Fourth, at the end of the loading cycle, both sheets move following the trajectory outlined by their anchor points (Figures 1C(ii),D(ii)). Consequently, upon cyclic actuation, Design I crawls toward the left (Figure 1C(iii); and Movie S2, Supporting Information), while Design II moves straight (Figure 1D(iii); and Movie S3, Supporting Information).

The results of Figure 1C,D underscore the potential of exploiting the nonlinear kinematics of the origami sheets for locomotion, albeit with each design limited to a predefined trajectory. However, it is important to note that certain origami sheets offer opportunities for motion along arbitrary trajectories. As an example, in Figure 1E, we present results for an origami sheet (Design III) with $b = 90$ mm, $h = 135$ mm, $(x_v, y_v) = (27, 36)$ mm, and (θ_1, θ_2, θ_3, θ_v)=(140°, 100°, 60°, 60°). We find that for $157° \leqslant \beta \leqslant 163°$ this origami sheet moves forward upon cyclic actuation, while for $130° \leqslant \beta \leqslant 135°$ it turns left (see Movie S4, Supporting Information). This change in locomotion is due to a shift in contact points. For $\beta > 155°$, an edge and a vertex of the sheet are in contact with the substrate (highlighted by red markers in Figure 1E). However, when β decreases below 155°, the shape change causes the origami device to establish new contact points at the three edges of the origami sheet (also highlighted by red markers in Figure 1E). This shift in contact points changes the anchor point and, therefore, leads to a different crawling mode.

Next, we develop a quasi-static model to systematically explore how the fold arrangement within the origami sheet affects its crawling trajectory. While an origami sheet itself is a single-degree-of-freedom mechanism, its interactions with the substrate introduce three additional degrees of freedom: the components of displacement of its center of mass in the plane of the substrate, and the rotation around an axis perpendicular to the substrate. Since these degrees of freedom are controlled by friction, predicting the trajectory traced by the origami sheet requires determining the frictional forces. To this end, we first introduce an equivalent spherical linkage to derive explicit equations describing the kinematics of the origami sheet as a function of the folding angle β.[38] We then numerically identify the three vertices in contact with the substrate upon actuation (see Sections S3A–C, Supporting Information for details). Once the contact points and folded configurations are determined, we impose equilibrium to calculate the normal forces at the contact points, N, and then compute the static friction forces at each contact point as:

$$F^s = \mu^s(\psi)N \tag{1}$$

where μ^s is the experimentally measured static coefficient of friction, which depends on the angle formed by the face of the origami in contact and the substrate, ψ (see Sections S2B, Supporting Information).

As an example, in **Figure 2A–B**, we show the predicted folded configurations, contact points, and evolution of frictional forces for Design III. Our model, consistent with our experiments, predicts a shift in contact points. Specifically, for $\beta \geqslant 155°$, the model predicts that one edge (v_3-v_6) and one corner (v_8) will be in contact with the substrate, whereas for $\beta < 155°$, there are three point contacts (v_6, v_8, v_9). According to our model, for $\beta \geqslant 155°$, the edge v_3-v_6 experiences higher static friction forces, while for $\beta < 155°$, the contact point v_6 bears a greater frictional force (Figure 2B).

Having determined the static frictional forces at the contact points, we proceed to calculate the tangential forces, $\mathbf{f}^t$ at these points. Although the system is statically indeterminate (with three equilibrium conditions to determine six unknown tangential force components - $f^t x$ and $f^t y$ at each of the three contact nodes), it is crucial to recognize that to achieve locomotion, one contact point must stick while the other two must slip. The sticking contact point must satisfy the sticking criterion:

$$|f^t| \leq \mu^s(\psi)N \tag{2}$$

whereas the slipping contact points must satisfy:

$$|f^t| = \mu^s(\psi)N \tag{3}$$

Therefore, an origami sheet can crawl upon actuation if the equilibrium equations are satisfied with two contact points meeting Equation (3) and one satisfying Equation (2). The latter acts as an anchor point, and we fix its in-plane coordinates to calculate the trajectory traced by the sheet as the pouch is deflated (see Section S3D, Supporting Information for details).

In Figures 2C,D, we present the predicted trajectory traced for Design III for a single cycle of actuation with $157° \leqslant \beta \leqslant 163°$ and $130° \leqslant \beta \leqslant 135°$, respectively. We observe that in the first case, the sheet moves almost straight, with the tangent to the curve changing by 0.56° over an 11.95 mm step size, while in the

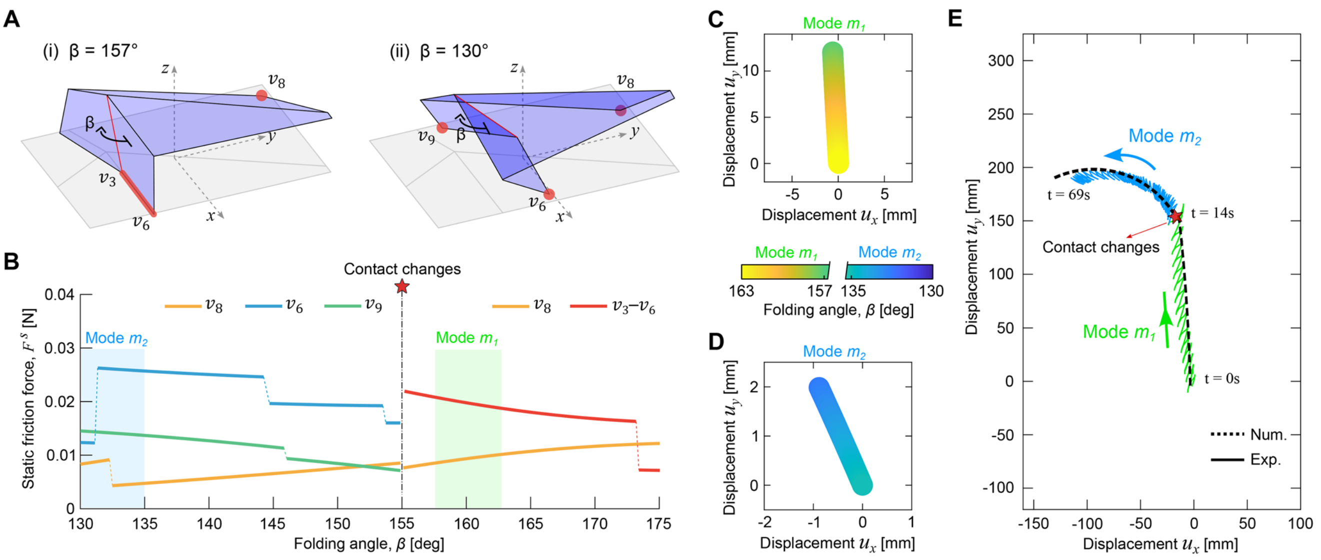

Figure 2. Comparison of experimental and numerical results for Design III. A) Numerically predicted location of contacts (highlighted in red) for $\beta = 157°$ and 130°. B) Numerically predicted evolution of the static friction forces at the contact nodes as a function of folding angle β. The ranges of β used in the tests shown in Figure 1E to move straight and turn are indicated by the green and blue shaded areas, respectively. C,D) Numerically predicted displacement of the center of mass of the sheet for a complete actuation cycle with (C) $157° \leqslant \beta \leqslant 163°$ and (D) and $130° \leqslant \beta \leqslant 135°$. E) Comparison of the numerically predicted (dashed line) and experimentally observed (continuous line) trajectory traced by Design III when subjected to 14 loading cycles with $157° \leqslant \beta \leqslant 163°$ followed by 55 loading cycles with $130° \leqslant \beta \leqslant 135°$.

second case, the tangent to the curve changes by 1.5° over only a 2.14 mm step size, initiating a turning movement. Upon cyclic actuation, the first scenario results in a straight trajectory, whereas the second scenario leads to a turning motion (see Figure 2E). Both outcomes align well with the experimental results, with minor discrepancies attributed to uncertainties in measuring the folding angle, slippage of the anchor point during deflation, and not accounting for centroid displacement during inflation.

Having established a model that accurately captures the trajectory of our origami sheets upon actuation, we then use it to systematically explore the design space. To this end, we investigate the response of more than two million sheets with $b = 90$ mm, $h \in [1, 1.5]b$, $\theta_i \in [20°, 30°, 40°, ..., 170°]$, $\theta_v \in [10°, 30°, 50°, ..., 350°]$, $x_v \in [-0.7, -0.5, -0.3]b$ and $y_v \in [-1.2, -1, -0.8, -0.6, -0.4]b$. In our analyses, the folding angle β is initially decreased from 180° to 120° and then returned to 180° in increments of 0.5°. Out of the 579,215 designs that are rigidly foldable, we find that 243,067 fail to achieve locomotion due to their inability to stand (indicated by negative normal forces), facet collisions during folding (where dihedral angles at mountain folds reach 2π), or the absence of an anchor point during deflation. To rationalize the behavior of the remaining 336,148 designs that do crawl, we calculate the local curvature κ of the predicted trajectory during deflation. We classify a portion of the trajectory as straight if $\kappa < 5 \times 10^{-3}$ mm^{-1}, and as curved otherwise, using the angle formed by the tangent to the trajectory with the horizontal axis to distinguish between left and right turns (see **Figure 3A**; Section S3F, Supporting Information for details).

As shown in Figure 3B, we find that many designs support multiple distinct crawling modes. Some achieve multimodal crawling without altering their anchor point ($N_{\text{change}} = 0$), solely leveraging their nonlinear kinematics. In contrast, others utilize changes in contact points to vary their crawling mode (note that designs with $N_{\text{change}} > 2$ are disregarded as they typically result in inefficient locomotion). The former results in a continuous trajectory characterized by a broad range of κ, while the latter exhibits discontinuous transition points along the trajectory (Figure 3A). Among the 229,073 designs with $N_{\text{change}} < 2$, 47.77% can support only one crawling mode. Specifically, 25.89% move

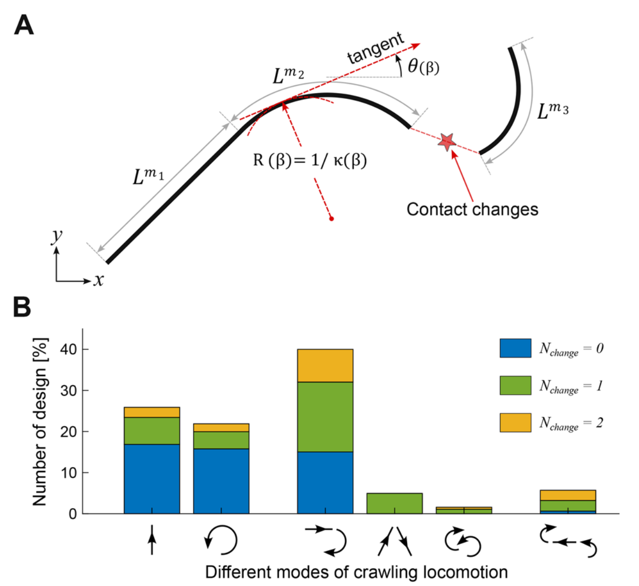

Figure 3. Parametric study. A) Schematic of a typical trajectory for the center of mass of an origami sheet upon a loading cycle. B) Classification of the considered 229,073 designs based on their supported crawling modes. Bar colors indicate the number of contact changes, N_{change}.

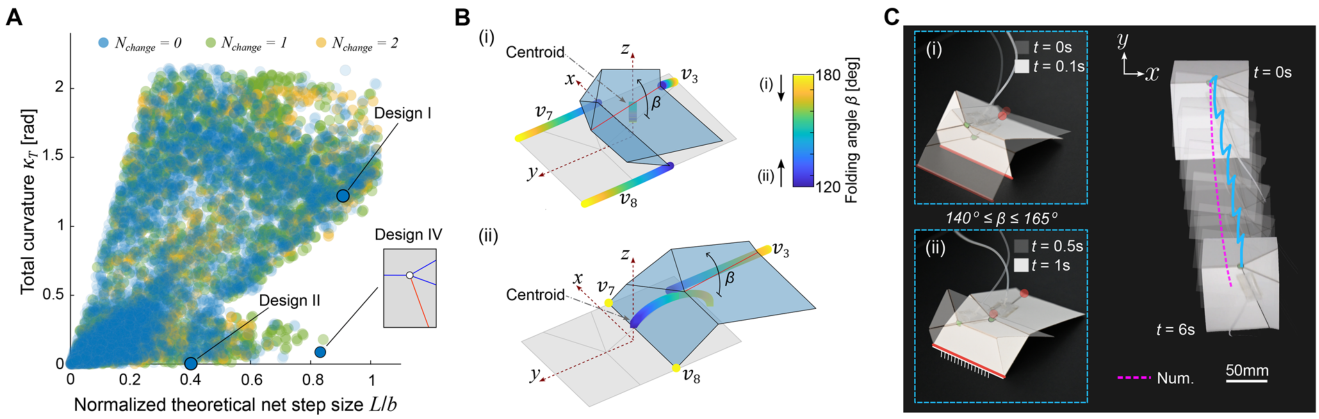

Figure 4. Designs supporting a single mode of crawling. A) Normalized net step size, L/b, versus total curvature κ_T (rad) for all designs supporting a single mode of crawling. Marker colors indicate the number of contact changes through a loading cycle, N_{change} B) Numerically predicted evolution of the position of the contact point during i) inflation and ii) deflation for Design IV. C) Snapshots of Design IV at different times during a loading cycle and frames from videos recorded during tests in which the sample is subjected to multiple inflation/deflation cycles. The magenta dashed line indicates the numerically predicted trajectory.

exclusively straight, and 21.88% turn exclusively. Furthermore, 46.52% of the designs support two modes of crawling: 40% move both straight and turn, 4.94% can turn left and right, and 1.58% move straight but can change direction. Finally, 5.71% of the designs exhibit three modes of crawling. By controlling the range of actuation of the folding angle, these designs can crawl straight, turn left, or turn right.

In **Figure 4**, we focus on designs that support only one crawling mode, most of which have $N_{\text{change}} = 0$. To evaluate the performance of these designs, we calculate the length of the trajectory they trace (L) and the total change in the angle of the tangent to the trajectory, which is equivalent to the total curvature (κ_T), as β changes from 120° to 180°. In Figure 4A, we report L/b and κ_T for all designs. The results indicate that both L and κ_T can change largely by tuning the geometry. Specifically, focusing on designs capable of crawling straight (i.e., designs with $\kappa_T \approx 0$), we find that the step size can be greatly increased compared to that of Design II reported in Figure 1. Our model predicts that a design with $h = 1.5b$, $(\theta_1, \theta_2, \theta_3, \theta_v) = (150°, 110°, 50°, 30°)$ and $(x_v, y_v) = (0.5, 1)b$ (which we refer to as Design IV) will effectively behave as a biped (Figure 4B), achieving $L = 0.83b$ (more than twice that of Design II) and $\kappa_T = 0.1$ (see Movie S5, Supporting Information). In Figure 4C, we show the experimental results for Design IV, which fully confirmed the numerical predictions in terms of both folding mode and trajectory. In our experiments, we pressurize the pouch attached to the valley fold to vary β between 140° and 165°. In each actuation cycle, the origami sheet moves by approximately 37.2 mm, which closely matches the model prediction of 42.1 mm. Consequently, this design requires only six actuation cycles to move approximately 225 mm, whereas Design II takes fifteen cycles to cover the same distance.

Our systematic exploration of the design space reveals that an origami sheet can not only move straight in one direction or turn but also support two different locomotion modes. These designs include those that can move both straight and turn (similar to Design III in Figure 1E), as well as designs that can either turn or move straight in two different directions. In **Figure 5**, we focus on designs that move straight with a step length L^{m_1} along a direction forming an angle α^{m_1} with the horizontal axis when $\beta^{m_1}_{min} < \beta < \beta^{m_1}_{max}$, and along a direction forming an angle α^{m_2} with steps of length L^{m_2} when $\beta^{m_2}_{min} < \beta < \beta^{m_2}_{max}$. Our model identifies 11,312 such designs, all with $N_{\text{change}} = 1$, and in Figure 5A, we show $\alpha = |\alpha^{m_1} - \alpha^{m_2}|$ and $L_{min}/b = \min(L^{m_1}, L^{m_2})/b$ for all of them. We find that the geometry of the sheets significantly affects both the step size and the angle between the two supported directions of motion. For example, for a design with $h = 1.5b$, $(\theta_1, \theta_2, \theta_3, \theta_v) = (100°, 100°, 60°, 20°)$, and $(x_v, y_v) = (0.7, 0.9)b$ (which we refer to as Design V), our model predicts $\alpha = 177°$ and $L_{min} = 0.12b$. In contrast, for a design with $h = 1.5b$, $(\theta_1, \theta_2, \theta_3, \theta_v) = (140°, 40°, 100°, 50°)$, and $(x_v, y_v) = (0.7, 0.4)b$ (which we refer to as Design VI), it predicts $\alpha = 38°$ and $L_{min} = 0.19b$. Note that for the former $(\beta^{m1}_{min}, \beta^{m1}_{max}, \beta^{m2}_{min}, \beta^{m2}_{max})$=(125°, 140°, 156°, 165°), while for the latter $(\beta^{m1}_{min}, \beta^{m1}_{max}, \beta^{m2}_{min}, \beta^{m2}_{max})$=(150°, 170°, 120°, 149°).

In Figure 5B, C, we report experimental results for Design V and Design VI, respectively. For Design V, we find that when $129° \leqslant \beta \leqslant 135°$, one edge and a corner are in contact with the substrate (highlighted in red in Figure 5 Bi). However, if $\beta > 155.4°$, the center of mass of the origami sheet falls outside the triangle formed by the contact points, causing it to tip over (Figure 5 Bii) and make contact with the substrate through three vertices (highlighted in red in Figure 5 Biii). In contrast, for Design VI, one edge and a corner are always in contact with the substrate, but the corner in contact changes at $\beta \approx 149°$ (highlighted in red in Figure 5C(i)-(ii)). These changes in contact make Design V and Design VI move along two straight lines separated by an angle $\alpha = 165°$ and 39°, respectively, when actuated within $\beta \in [\beta^{m1}_{min}, \beta^{m1}_{max}]$ and $\beta \in [\beta^{m2}_{min}, \beta^{m2}_{max}]$, see Movies S6 and S7 (Supporting Information). Thus, our experimental results confirm an effective change in the direction of motion by controlling the range of actuation for β.

Finally, in **Figure 6**, we consider designs that can move straight and turn in two different directions. These designs move straight with a step length L^{m_1} when $\beta^{m_1}_{min} < \beta < \beta^{m_1}_{max}$ and turn left and right with a step length L^{m_2} and L^{m_3} when $\beta^{m_2}_{min} < \beta < \beta^{m_2}_{max}$ and $\beta^{m_3}_{min} < \beta < \beta^{m_3}_{max}$, respectively. Our model identifies 13,070 such

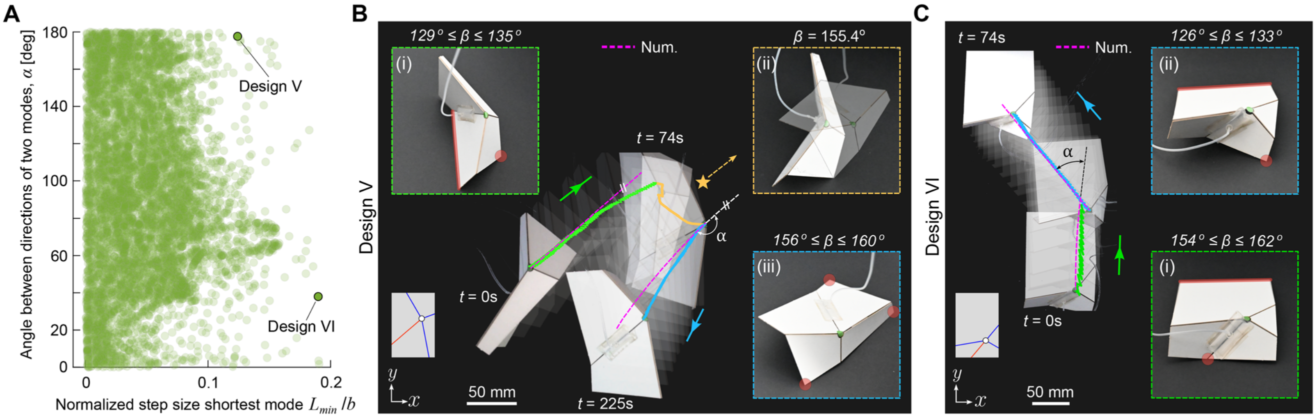

Figure 5. Designs capable of moving straight in two different directions. A) Angle between the two supported directions (α) versus normalized minimum step size (L_{min}/b) for all designs capable of moving straight in two different directions. B–C) Snapshots of (B) Design V and (C) Design VI at different times during a loading cycle, with frames from videos recorded during tests in which the samples are subjected to multiple inflation/deflation cycles. Magenta dashed lines indicate the numerically predicted trajectory.

designs, with 1,458 achieving this with $N_{\text{change}} = 0$, 5,913 with $N_{\text{change}} = 1$, and 5,699 with $N_{\text{change}} = 2$. In Figure 6A, we report $L_{\text{min}} = \min(L^{m_1}, L^{m_2}, L^{m_3})$ and $L_T = \sum_{i=1}^{3} L^{m_i}$ for all these designs. To highlight the combined contributions of contact changes and nonlinear kinematics, we aim to identify a crawler with $N_{\text{change}} = 1$ that can consistently achieve large step sizes across all three crawling modes. This requires maximizing both L_T and L_{min}. To this end, we select an origami sheet characterized by $h = 1.5b$, $(\theta_1, \theta_2, \theta_3, \theta_v) = (130°, 90°, 70°, 90°)$, and $(x_v, y_v) = (0.3, 1.2)b$, referred to as Design VII. Although a few other $N_{\text{change}} = 1$ designs showed slightly better performance in simulation, they were impractical for experimental testing. At large folding angles, the pneumatic tubing in these designs rubbed against the substrate, reducing reliability. Our model predicts that Design VII, with $N_{\text{change}} = 1$, has $L_T = 0.65b$ and $L_{\text{min}} = 0.17b$, indicating it can move with large steps both straight and when turning in either direction. In excellent agreement with the model, our experiments show that for $157° \leqslant \beta \leqslant 162°$, three vertices are in contact with the substrate (highlighted in red in Figure 6B(i)), resulting in a left-turn crawling motion (green portion of the trajectory in Figure 6B). However, at $\beta \leqslant 154°$, this contact configuration becomes unstable, and the sheet establishes new contact with the substrate through an edge and a vertex (highlighted in red in Figure 6B(iii)). This change in contact configuration allows Design VII to crawl in a straight line when actuated within the range $135° \leqslant \beta \leqslant 139°$ for 67 cycles. Furthermore, when the range of actuation is increased to $140° \leqslant \beta \leqslant 152°$ (Figure 6B(iv)), a right-turn crawling motion is achieved with the same contact configuration due to the nonlinear kinematics of the origami (See Movie S8, Supporting Information). As such, these results confirm that both changes in contact and nonlinear kinematics can be exploited to control the crawling direction of origami sheets.

3. Discussion and Conclusion

In summary, we have demonstrated that the nonlinear kinematics of origami sheets can be exploited to realize a crawler capable of multimodal locomotion when actuated with a single input.

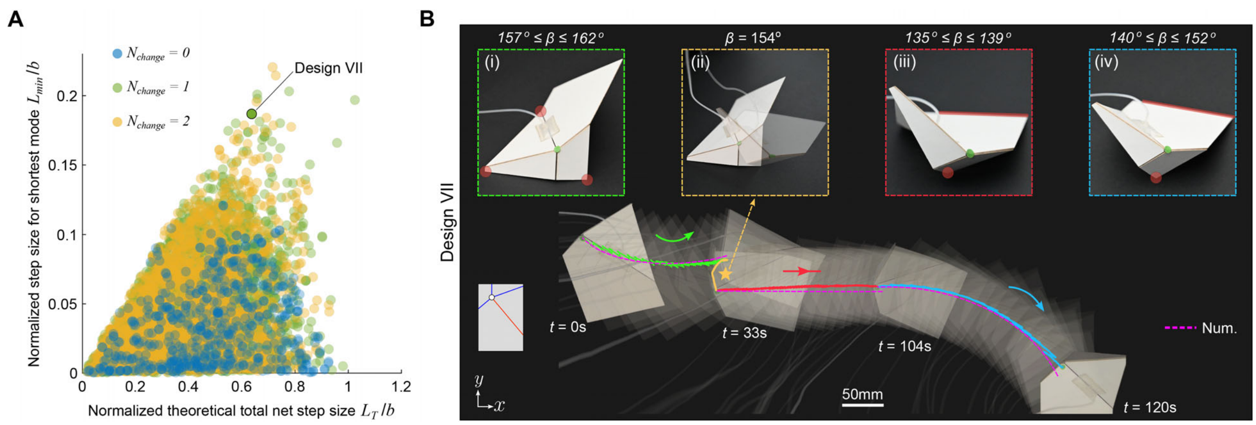

Figure 6. Designs supporting three modes of crawling. A) Normalized minimum step size L_{min}/b versus normalized total step size L_T/b for all designs supporting three modes of locomotion. Marker colors indicate the number of contact changes through a loading cycle, N_{change} B) Snapshots of Design vII at different times during a loading cycle and frames from videos recorded during tests in which the sample is subjected to multiple inflation/deflation cycles. The magenta dashed line indicates the numerically predicted trajectory.

ADVANCED MATERIALS
www.advmat.de

We specifically considered one of the simplest origami building blocks – a rigid degree-four vertex – and identified designs that can move straight and turn both left and right by simply controlling the range of folding for the actuated fold. Our results show multimodal behavior arising through three distinct mechanisms i) Shape–substrate contact change: A change in the set of contact points is triggered purely by the sheet's shape evolution and its interaction with a flat substrate (e.g., Designs III and VI). This transition is fully reversible: returning the folding angle β to its original range restores the initial contact set and the crawler's previous gait. ii) Tipping-induced contact change: when the center of mass crosses the boundary of the support tripod, the sheet tips over, and a new set of contacts is established (e.g., Design V and the left-turn → straight switch in Design VII). Once tipped, the sheet remains on the new configuration; the transition is therefore not reversible under normal actuation unless the crawler is manually reset. iii) Non-linear kinematics and unchanged contact nodes: With the contact set unchanged, nonlinear folding kinematics alone yield different gaits depending on the actuation range (e.g., the straight ↔ right-turn switch in Design VII). This approach is reversible: changing the β range suffices to toggle between modes.

While this study focused on crawling, the rich nonlinear mechanics of origami could be further exploited to achieve other locomotion gaits, such as walking, swimming, rolling, and jumping. For instance, transitioning to a circular or curved boundary could enable rolling locomotion by continuously relocating the center of mass.[39] Additionally, it has been shown that a simple degree-four vertex can be programmed to be multistable.[36] The rapid movements triggered by snapping in multistable designs could potentially be used to make the origami sheets jump.[40,41] Moreover, multistability could allow for hysteresis-dependent path generation, creating asymmetrical ellipsoidal gaits, and opening up possibilities for walking and swimming locomotion gaits.

In this study, we use a single-chamber inflatable pouch sized to the facet, which limited the folding range closing from 180° to 125° and the actuation frequency to about 1 Hz. Increasing the pouch width can produce a larger folding range, where the folding angle β can close from 180° to 85°.[42] A larger folding range yields a larger step size, broadens the design space, and enables more complex behavior. However, they come with trade-offs: larger pouches respond more slowly due to the increased air volume that must be exchanged, and they are not suitable for all designs, as they require larger surface areas for attachment. To address these limitations and improve actuation performance, recently proposed strategies can be employed. For instance, cascading multiple pouches can achieve an even greater range, closing β toward 0°,[43] while incorporating kinking mechanisms can accelerate actuation.[44] In addition, recent advances in smart and active soft materials, such as shape memory polymers,[45] liquid crystal elastomers,[46,47] magnetic elastomers,[48,49] and dielectric elastomers,[50] could be leveraged to integrate actuation directly into the folding mechanisms. Although our crawlers operate predominantly in open-loop mode, incorporating emerging stimuli-responsive materials[51,52] would enable greater adaptability and facilitate closed-loop control. In addition, the flat origami platform can be scaled and integrated with soft, miniaturizable actuation schemes[53] to perform small-scale robotic tasks. By leveraging these materials for both actuation and sensing, future untethered systems will gain enhanced performance and versatility, paving the way for more complex robotic applications.

4. Experimental Section

Details of the design, materials, and fabrication methods are summarized in Sections S1, S2, and S3 (Supporting Information). The fabrication process is detailed in Section S1 (Supporting Information). The experimental procedures, including actuation procedures, testing for the static coefficient of friction, and the pressure-volume relationship of the inflatable pouch motor, are described in Section S2 (Supporting Information). The numerical model to predict the locomotion behavior of a generic degree-four origami vertex is detailed in Section S3 (Supporting Information). This included the geometric description, crawling locomotion analysis, comparison of numerical and experimental results, and the results from the parametric study.

Supporting Information

Supporting Information is available from the Wiley Online Library or from the author.

Acknowledgements

D.F. acknowledged funding support from the Dutch Research Council under the NWO-ENW Rubicon grant agreement (019.191EN.022, 2019). The authors gratefully acknowledged support from the ARO MURI program (W911NF-22-1-0219) and the Simons Collaboration on Extreme Wave Phenomena Based on Symmetries.

Conflict of Interest

The authors declare no conflict of interest.

Data Availability Statement

The data that support the findings of this study are available in the supplementary material of this article.

Keywords

degree-four vertex, locomotion, origami, robotics

Received: February 3, 2025
Revised: May 12, 2025
Published online:

[1] E. Hawkes, B. An, N. M. Benbernou, H. Tanaka, S. Kim, E. D. Demaine, D. Rus, R. J. Wood, *Proc. Nat. Acad. Sci.* **2010**, *107*, 12441.
[2] S. A. Zirbel, R. J. Lang, M. W. Thomson, D. A. Sigel, P. E. Walkemeyer, B. P. Trease, S. P. Magleby, L. L. Howell, *J. Mech. Des.* **2013**, *135*, 111005.
[3] E. T. Filipov, T. Tachi, G. H. Paulino, *Proc. Natl. Acad. Sci.* **2015**, *112*, 12321.

[4] T. G. Nelson, A. Avila, L. L. Howell, J. L. Herder, D. F. Machekposhti, *Mech. Mach. Theory* **2019**, *140*, 194.
[5] D.-Y. Lee, J.-K. Kim, C.-Y. Sohn, J.-M. Heo, K.-J. Cho, *Sci. Rob.* **2021**, *6*, eabe0201.
[6] D. Melancon, B. Gorissen, C. J. García-Mora, C. Hoberman, K. Bertoldi, *Nature* **2021**, *592*, 545.
[7] J. L. Silverberg, A. A. Evans, L. McLeod, R. C. Hayward, T. Hull, C. D. Santangelo, I. Cohen, *science* **2014**, *345*, 647.
[8] M. Schenk, S. D. Guest, *Proc. Natl. Acad. Sci.* **2013**, *110*, 3276.
[9] E. Boatti, N. Vasios, K. Bertoldi, *Adv. Mater.* **2017**, *29*, 1700360.
[10] B. Treml, A. Gillman, P. Buskohl, R. Vaia, *Proc. Natl. Acad. Sci.* **2018**, *115*, 6916.
[11] Z. Liu, H. Fang, J. Xu, K.-W. Wang, *Adv. Intell. Syst.* **2023**, *5*, 2200146.
[12] K. Y. Ma, P. Chirarattananon, S. B. Fuller, R. J. Wood, *Science* **2013**, *340*, 603.
[13] S. M. Felton, M. T. Tolley, C. D. Onal, D. Rus, R. J. Wood, in *2013 IEEE International Conference on Robotics and Automation*, IEEE, Piscataway, NJ **2013**, pp. 277–282.
[14] S. Felton, M. Tolley, E. Demaine, D. Rus, R. Wood, *Science* **2014**, *345*, 644.
[15] D. Rus, M. T. Tolley, *Nat. Rev. Mater.* **2018**, *3*, 101.
[16] Q. Liu, W. Wang, M. F. Reynolds, M. C. Cao, M. Z. Miskin, T. A. Arias, D. A. Muller, P. L. McEuen, I. Cohen, *Sci. Rob.* **2021**, *6*, eabe6663.
[17] W. Yan, S. Li, M. Deguchi, Z. Zheng, D. Rus, A. Mehta, *Nat. Commun.* **2023**, *14*, 1553.
[18] Z. E. Teoh, B. T. Phillips, K. P. Becker, G. Whittredge, J. C. Weaver, C. Hoberman, D. F. Gruber, R. J. Wood, *Sci. Rob.* **2018**, *3*, eaat5276.
[19] J.-S. Koh, K.-J. Cho, *IEEE/ASME Trans. Mech.* **2012**, *18*, 419.
[20] C. D. Onal, R. J. Wood, D. Rus, *IEEE/ASME Trans. Mech.* **2012**, *18*, 430.
[21] W. Kim, J. Byun, J.-K. Kim, W.-Y. Choi, K. Jakobsen, J. Jakobsen, D.-Y. Lee, K.-J. Cho, *Sci. Rob.* **2019**, *4*, eaay3493.
[22] P. Bhovad, S. Li, *Sci. Rep.* **2021**, *11*, 13002.
[23] Q. Ze, S. Wu, J. Nishikawa, J. Dai, Y. Sun, S. Leanza, C. Zemelka, L. S. Novelino, G. H. Paulino, R. R. Zhao, *Sci. Adv.* **2022**, *8*, eabm7834.
[24] R. F. Shepherd, F. Ilievski, W. Choi, S. A. Morin, A. A. Stokes, A. D. Mazzeo, X. Chen, M. Wang, G. M. Whitesides, *Proc. Natl. Acad. Sci.* **2011**, *108*, 20400.
[25] S. D. De Rivaz, B. Goldberg, N. Doshi, K. Jayaram, J. Zhou, R. J. Wood, *Sci. Rob.* **2018**, *3*, eaau3038.
[26] S. Wu, T. Zhao, Y. Zhu, G. H. Paulino, *Proc. Natl. Acad. Sci.* **2024**, *121*, e2322625121.
[27] G.-Z. Yang, J. Bellingham, P. E. Dupont, P. Fischer, L. Floridi, R. Full, N. Jacobstein, V. Kumar, M. McNutt, R. Merrifield, B. J. Nelson, B. Scassellati, M. Taddeo, R. Taylor, M. Veloso, Z. L. Wang, R. Wood, *Sci. Rob.* **2018**, *3*, eaar7650.
[28] W. Hu, G. Z. Lum, M. Mastrangeli, M. Sitti, *Nature* **2018**, *554*, 81.
[29] Q. Ze, S. Wu, J. Dai, S. Leanza, G. Ikeda, P. C. Yang, G. Iaccarino, R. R. Zhao, *Nat. Commun.* **2022**, *13*, 3118.
[30] W.-K. Lee, D. J. Preston, M. P. Nemitz, A. Nagarkar, A. K. MacKeith, B. Gorissen, N. Vasios, V. Sanchez, K. Bertoldi, L. Mahadevan, G. M. Whitesides, *Sci. Rob.* **2022**, *7*, eabg5812.
[31] D. Drotman, S. Jadhav, D. Sharp, C. Chan, M. T. Tolley, *Sci. Rob.* **2021**, *6*, eaay2627.
[32] D. Zarrouk, R. S. Fearing, in *2014 IEEE International Conference on Robotics and Automation (ICRA)*, IEEE, Piscataway, NJ **2014**, pp. 2569–2569.
[33] S. Noji, S. Nansai, N. Kamamichi, H. Itoh, *IEEE Robot. Autom. Lett.* **2022**, *7*, 6399.
[34] D. Feshbach, X. Wu, S. Vasireddy, L. Beardell, B. To, Y. Baryshnikov, C. Sung, in *2023 IEEE/RSJ International Conference on Intelligent Robots and Systems (IROS)*, IEEE, Piscataway, NJ **2023**, pp. 2485–2492.
[35] Z. Abel, J. Cantarella, E. D. Demaine, D. Eppstein, T. C. Hull, J. S. Ku, R. J. Lang, T. Tachi, *J. Comp. Geom.* **2016**, *7*, 171.
[36] S. Waitukaitis, R. Menaut, B. G.-g. Chen, M. Van Hecke, *Phys. Rev. Lett.* **2015**, *114*, 055503.
[37] S. Waitukaitis, M. Van Hecke, *Phys. Rev. E* **2016**, *93*, 023003.
[38] J. Denavit, R. S. Hartenberg, *J. Appl. Mech.* **1955**, *22*, 215.
[39] Y. I. Sobolev, R. Dong, T. Tlusty, J.-P. Eckmann, S. Granick, B. A. Grzybowski, *Nature* **2023**, *620*, 310.
[40] B. Gorissen, D. Melancon, N. Vasios, M. Torbati, K. Bertoldi, *Sci. Rob.* **2020**, *5*, eabb1967.
[41] Y. Chi, Y. Li, Y. Zhao, Y. Hong, Y. Tang, J. Yin, *Adv. Mater.* **2022**, *34*, 2110384.
[42] R. Niiyama, X. Sun, C. Sung, B. An, D. Rus, S. Kim, *Soft Rob.* **2015**, *2*, 59.
[43] S. Oka, K. Koyama, T. Gondo, Y. Ikeda, Y. Kawahara, K. Narumi, in *Extended Abstracts of the CHI Conference on Human Factors in Computing Systems*, Association for Computing Machinery (ACM), Honolulu, HI, USA, **2024**, pp. 1–4.
[44] A. Comoretto, H. A. H. Schomaker, J. T. B. Overvelde, *Science* **2025**, *388*, 610.
[45] Y. Xia, Y. He, F. Zhang, Y. Liu, J. Leng, *Adv. Mater.* **2021**, *33*, 2000713.
[46] A. Kotikian, C. McMahan, E. C. Davidson, J. M. Muhammad, R. D. Weeks, C. Daraio, J. A. Lewis, *Sci. Rob.* **2019**, *4*, eaax7044.
[47] H. Zeng, P. Wasylczyk, C. Parmeggiani, D. Martella, M. Burresi, D. S. Wiersma, *Adv. Mater. (Deerfield Beach, Fla.)* **2015**, *27*, 3883.
[48] J. Cui, T.-Y. Huang, Z. Luo, P. Testa, H. Gu, X.-Z. Chen, B. J. Nelson, L. J. Heyderman, *Nature* **2019**, *575*, 164.
[49] J. Zhang, Y. Guo, W. Hu, M. Sitti, *Adv. Mater.* **2021**, *33*, 2100336.
[50] Y. Sun, D. Li, M. Wu, Y. Yang, J. Su, T. Wong, K. Xu, Y. Li, L. Li, X. Yu, J. Yu, *Microsyst. Nanoeng.* **2022**, *8*, 37.
[51] C. Ohm, M. Brehmer, R. Zentel, *Adv. Mater.* **2010**, *22*, 3366.
[52] A. Kotikian, R. L. Truby, J. W. Boley, T. J. White, J. A. Lewis, *Adv. Mater.* **2018**, *30*, 1706164.
[53] L. Hines, K. Petersen, G. Z. Lum, M. Sitti, *Adv. Mater.* **2017**, *29*, 1603483.